Subinertial Oscillations on the Amundsen Sea Shelf, Antarctica

A. K. WÅHLIN, O. KALÉN, AND K. M. ASSMANN

Department of Marine Sciences, University of Gothenburg, Göteborg, Sweden

E. DARELIUS

Geophysical Institute, University of Bergen, and Bjerknes Centre for Climate Research, Bergen, Norway

H. K. HA

Department of Ocean Sciences, Inha University, Incheon, South Korea

T. W. KIM AND S. H. LEE

Korea Polar Research Institute, Incheon, South Korea

(Manuscript received 29 December 2014, in final form 15 July 2015)

ABSTRACT

Mooring data from the western flank of Dotson trough, Amundsen Sea shelf region, show the presence of barotropic oscillations with a period of 40–80 h. The oscillations are visible in velocity, temperature, salinity, and pressure and are comparable to tides in magnitude. The period of the oscillations corresponds to topographic Rossby waves of low group velocity and a wavelength of about 40 km, that is, the half-width of the channel. It is suggested that these resonant topographic Rossby waves cause the observed peak in the wave spectra. The observations show that sparse CTD data from this region should be treated with caution and need to be complemented with moorings or yo-yo stations in order to give a representative picture for the hydrography.

1. Introduction

Rapidly melting ice shelves and inflow of warm water on the continental shelf sea in the Amundsen Sea have brought attention and increased research activity to the region, and the knowledge about the circulation in the area has increased substantially over the last decade. Figure 1 shows a partial map of the Amundsen shelf area. It is crosscut by two deep troughs: the Pine Island trough that branches out in two distinct exits and the Dotson trough with one main exit on the shelf break. These troughs channel relatively warm and salty water southward (Wåhlin et al. 2010; Walker et al. 2007) from the deep ocean toward the floating glaciers at the coast where it induces basal melt (e.g., Jenkins et al. 2010; Jacobs et al. 2011). The focus of this paper is the Dotson trough, where records from two current meter moorings (Fig. 1 and Table 1) deployed on the flanks of the trough reveal a persistent inflow of warm and salty deep water (Wåhlin et al. 2010; Arneborg et al. 2012; Wåhlin et al. 2013; Ha et al. 2014) on the eastern flank and an outflow of colder and fresher product waters on the western flank (Ha et al. 2014). The circulation pathway of the deep water (thick lines with arrows in Fig. 1) was investigated by Ha et al. (2014), and it was shown that the inflow has velocity-weighted average temperature of about 0.75°C and salinity 34.6 psu. From budget calculations based on the mooring data, it was found that the outflow current was 1.25°C colder and 0.3 psu fresher than the inflow because of the mixing with glacial meltwater, which corresponds to the melting of about 80–240 km^3 of glacial ice per year. The overturning time was estimated to 4 months. In both moorings, a

Denotes Open Access content.

Corresponding author address: Dr. A. K. Wåhlin, Department of Earth Sciences, University of Gothenburg, P.O. Box 460, 40530 Göteborg, Sweden.
E-mail: awahlin@gu.se

DOI: 10.1175/JPO-D-14-0257.1

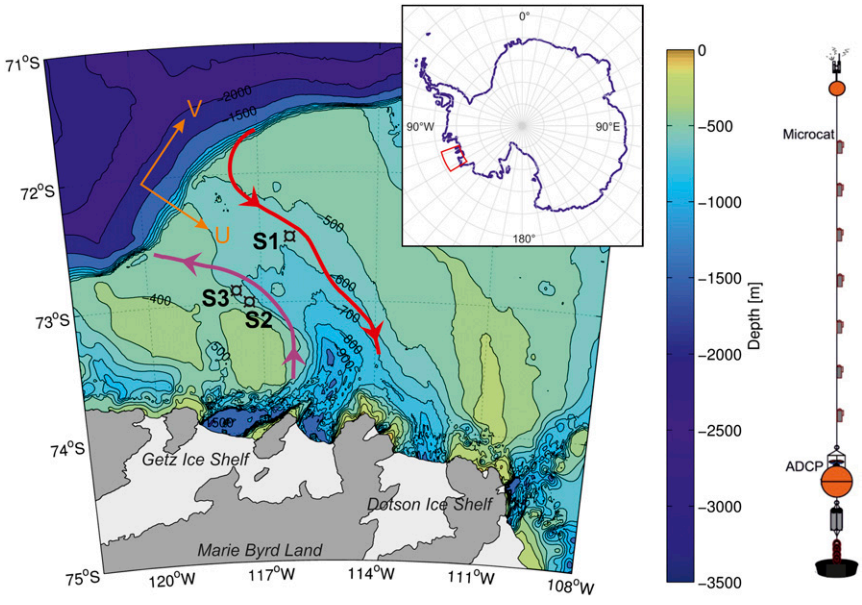

FIG. 1. (left) Map of the study region with the moorings S1, S2, and S3 and (right) the mooring design. The orange arrows show the rotation of the velocities to fit the orientation of the channel, with U as the along-trough velocity and V the cross-trough velocity. The red and purple lines with arrows depict the general circulation pattern and cooling of the warm deep water (Ha et al. 2014). Bathymetry is from Arndt et al. (2013). The inset shows the location of the study region in Antarctica.

strong short-term variability dominates the time dependence in velocity, temperature, and salinity. On the eastern flank the velocity varied on time scales from subtidal to monthly, was correlated with eastward wind at the shelf break (Wåhlin et al. 2013), and had no pronounced seasonality. A weak wintertime maximum in the bottom temperature and CDW layer thickness was, however, observed that was not related to the velocity (Wåhlin et al. 2013; Ha et al. 2014).

The focus of this work will be the quasi-regular oscillations with a period of about 2.5 days that are found at the site of a mooring located on the western flank of the trough, that is, the outflow side. The instantaneous velocity and hydrography is dominated by these oscillations. It is suggested that the oscillations are due to resonant topographic Rossby waves, which have previously been observed, for example, on the Scottish continental shelf (Gordon and Huthnance 1987) and on the southern slope of the Iceland–Faroe Ridge (Miller et al. 1996).

Topographic Rossby waves are a manifestation of conservation of potential vorticity; a water column forced to move across isobaths acquires relative vorticity (rotation) as it is stretched or squeezed. In the Southern Hemisphere, the phase of topographic Rossby waves propagates with shallow water on the left, while the energy of the wave follows the group velocity, which may be directed either to the right or to the left depending on the wavelengths (Gill 1982). For lower modes of the wave the dispersion curve typically displays a local maximum, with the group velocity of short waves directed with shallow water on the right and the group velocity of longer waves with shallow water on the left. For some intermediate wavelength, the group velocity is zero or close to zero. The energy of the latter waves will hence remain in the forcing region. These zero group velocity waves are said to be resonant, and such waves have been observed to be generated, for example, by strong winds (Gordon and Huthnance 1987) or by tides (Padman et al. 1992).

TABLE 1. Mooring: coordinates, depth, deployment periods, and instrumentation. The ADCP's were both 150-kHz instruments from RDI deployed upward looking at the bottom to measure current velocity profiles. The observed velocity data were processed using the WinADCP software. The MicroCATs on S3 unfortunately stopped recording data in January 2013.

Mooring	Lat	Long	Depth (m)	Deployed	Recovered	ADCP	MicroCATs
S1	72°27.279′S	116°20.92′W	584	15 Feb 2010	1 Mar 2012	Y	5–7
S2	73°0.94′S	117°14.86′W	614	25 Dec 2010	11 Feb 2012	Y	6
S3	72°55.60′S	117°34.75′W	578	1 Mar 2012	25 Jan 2014	N	3

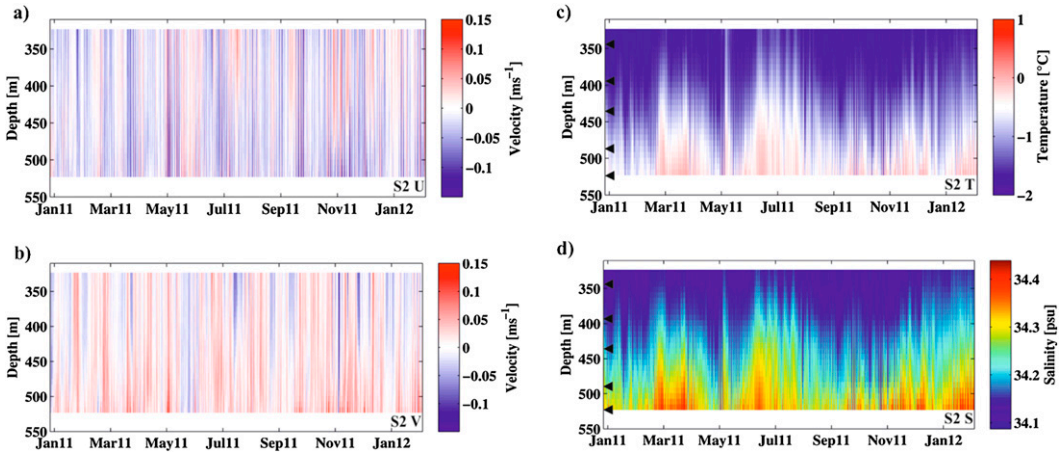

FIG. 2. Velocity, temperature, and salinity from mooring S2. The four panels show hourly averaged data according to color bars as a function of time and depth. (a) Detided along-channel velocity (positive in the southeastward direction, i.e., toward the continent), (b) detided across-channel velocity (positive in the northeastward direction, i.e., down the slope), (c) temperature, and (d) salinity. Black triangles in (c) and (d) show the approximate positions of the MicroCATs.

Rossby waves are not eddies, and they do not transport any fluid. The streamlines are per definition closed. Hence, they are not expected to influence transport of quantities such as heat or salt across the topography. The exception is when the waves are broken, for example, by small-scale topography (e.g., St-Laurent et al. 2013), in which case a net flow can occur. Eddies on the other hand can translate and move fluid parcels, and they are in some regions (e.g., the Antarctic fronts) the main mechanism that induces horizontal mixing and transport properties such as heat and salt laterally (e.g., Thompson 2008; Thompson et al. 2014). In similarity with Rossby waves, eddies can give an oscillating signal in hydrographic measurements. Since they are fundamentally different with regard to whether they induce net motion of the fluid or not, it is important to distinguish the two mechanisms. The present results indicate that topographic Rossby waves are very frequently, in fact almost constantly, present in the western part of the outer Amundsen shelf area. These waves will likely contaminate any measurements made in this area, indicating that single CTD and LADCP measurements from this region are of limited value.

2. Data

The data presented in this study were collected during two cruises with Icebreaker (IB) *Oden* during austral summer 2009/10 and 2010/11 and two cruises with RVIB *Araon* during 2011/12 and 2013/14. Three bottom-mounted subsurface moorings were placed in the western trough (Dotson trough) crossing the Amundsen Sea shelf. Figure 1 shows a map of the region, the location of the three moorings (for exact position and times in water, see Table 1), and the mooring setup. The position of mooring S1 was in the center of the warm inflow, while S2 and S3 were positioned in the outflow zone on the western flank. The mooring lines contained between three and seven MicroCATs (Seabird, SBE-37SMP) that measured temperature (with an accuracy of 0.002 K), conductivity (with an accuracy of 0.0003 S m^{-1}), and pressure (with an accuracy of 0.1 dbar). Two of the moorings also included an upward-looking 150-kHz acoustic Doppler current profiler (ADCP, RDI), deployed at the bottom to measure current velocity profiles. The observed velocity data were processed using the WinADCP software, removing data with error velocity exceeding 1.5 cm s^{-1} and beam correlation below 100. Fourier spectra were calculated using hourly time series and 50% overlapping Hanning windows with a length of 1024 h. The wind data used was the 6-h ERA-Interim product (Dee et al. 2011), which according to Bracegirdle and Marshall (2012) is the most accurate of the six major meteorological reanalysis products covering the Amundsen Sea. Bracegirdle and Marshall (2012) found generally good agreement between the ERA-Interim and independent data in the Bellingshausen Sea, and in Wåhlin et al. (2013) a good agreement was found between ERA-Interim and in situ data from Lindsey Island.

3. Observations

The primary focus here is mooring S2, deployed for 1 yr and equipped with an ADCP and five MicroCATs. Figure 2 shows the S2 temperature, salinity, and channel-rotated (i.e., with a rotation angle of 30° counterclockwise)

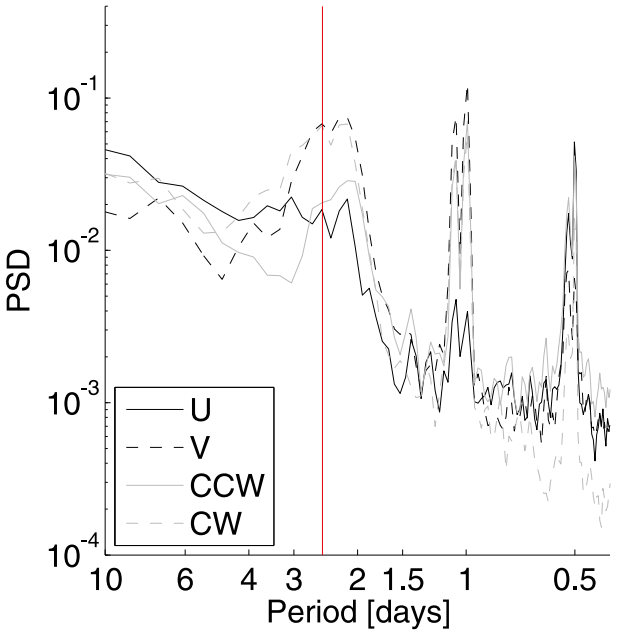

FIG. 3. Fourier spectra (black lines) and rotary spectra (gray lines) of velocity data from S2, 100 meters above the bottom (mab). Red line shows the frequency for zero group velocity according to the numerical model in Brink (2006).

velocities. Similar to S1 (Wåhlin et al. 2013) there is a pronounced short-term variability in all these quantities that dominates the instantaneous fields. The bottom temperature can vary by up to 1°C over less than a day, and the velocity can vary by 15 cm s^{-1} in that time span. The velocity fluctuations are nearly constant in the vertical, and there is a weak wintertime maximum in bottom temperature. The long time-mean along-channel velocity at S2 is an outflow of 2.5 cm s^{-1}, while the cross-channel component is weaker with a mean southwestward flow of less than 1 cm s^{-1} (Ha et al. 2014).

Figure 3 shows the Fourier spectra and the rotary spectra for the velocity at 100 m above bottom at S2. The velocity spectrum has marked peaks at the tidal frequencies and at the inertial frequency and a broad peak centered around period 40–80 h. The shape and relative magnitude of the broad peak is approximately equal for all measured parameters at S2 (velocity, temperature, and salinity). The oscillation is more energetic in the across-trough direction and mainly clockwise (Fig. 3).

To illustrate the temporal variation of the spectrum, wavelet analysis [according to Torrence and Compo (1998)] was used. Figure 4 shows the wavelet power spectra of bottom temperature and the vertically averaged velocities at S2. The peak around 40–80 h is present in the vertically averaged velocities (Figs. 4a,b) as well as bottom temperature (Fig. 4c). The energy peak is present during the whole measurement period, and a few shorter periods with elevated energy can also be detected. The characteristics of these periods are largely similar. Figure 5 shows an example, a detailed view of the velocity and temperature starting at 6 May 2011 (arrow in Fig. 4). The oscillations are present in the whole water column below 330 m. Temperature cooscillates with velocity, with dropping temperatures associated with southwestward currents across the channel and rising temperatures associated with northeastward velocities, indicating that the warm-water layer close to the bottom is being moved up and down the slope by strong velocity oscillations. The oscillations have similar magnitude in both spatial directions.

Figure 6 shows the temperature from the three MicroCATs at mooring S3. In similarity with the temperature at S2, there is strong subinertial variability that dominates any instantaneous temperature measurements. The lower panels of Fig. 6 show two examples of temperature oscillations, resembling the event in Fig. 5. The power spectra from the three MicroCATs show a broad subinertial peak similar to the one in Fig. 3 but centered around somewhat longer periods, around 70–100 h.

To examine the coherence between wind and the S2 mooring velocity, the spectral coherence between the vertically averaged currents and the wind pseudostress was calculated using the multitaper method (Thomson 1982). The pseudostress was rotated in order to identify the angle with largest coherence. The maximum coherence of 0.69 (with confidence level 0.43) was found for the frequency 67 h and the wind angle close to the local cross-shelf direction.

4. Topographic Rossby waves

Figure 7a shows the topography of the western flank of the trough as measured by the multibeam on IB *Oden* during a cruise to the region in 2010 (Arndt et al. 2013; http://www.ibcso.org/data.html), together with a simplified topography $h(y)$ with a constant bottom slope α, that is,

$$h(y) = H_0 - \alpha y, \tag{1}$$

where $h(y)$ is the bottom elevation as a function of across-slope distance y, $H_0 = -250$ m, and $\alpha = 0.01$.

Free topographic Rossby waves can form and travel along sloping topography. The shape of the wave (the eigenfunction) depends on the shape of the topography and the lateral boundary conditions. For the simplified topography [(1)], plane waves of the form

$$\Psi = \Psi_0 \sin(kx + ly - \omega t), \tag{2}$$

where (k, l) are the wavenumbers in the (x, y) directions and ω is the frequency, are solutions to the linear

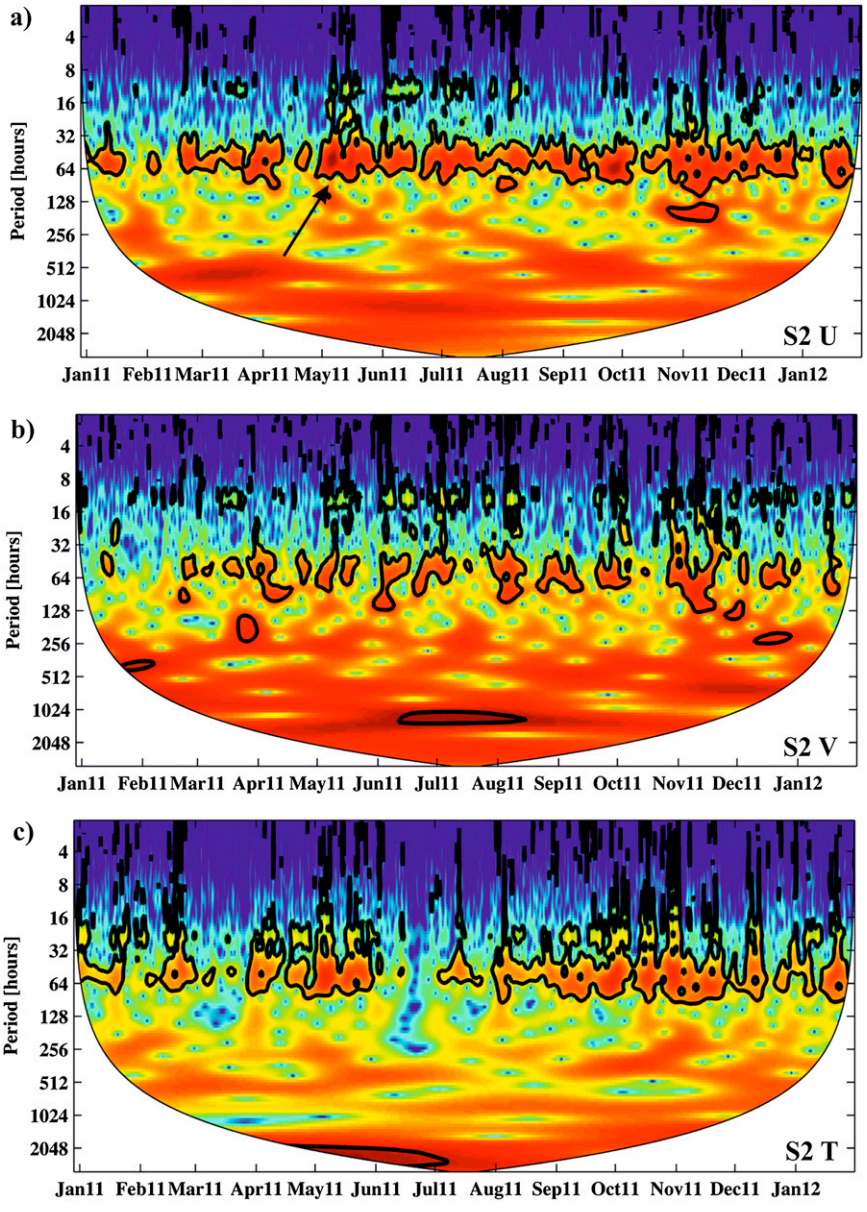

FIG. 4. Results from wavelet analysis of data from mooring S2: (a) along-channel velocity, vertical average; (b) across-channel velocity, and vertical average; and (c) temperature, bottom value. Red color indicates high energy levels and blue low levels. The thick black contours are the 95% confidence levels. Values outside cone of influence (parabolic black contour) are not plotted. The arrow in (a) shows the time of the oscillations in Fig. 5.

barotropic wave equation (Gill 1982). The dispersion relation is given by

$$\omega = -\frac{\beta k}{k^2 + l^2 + \dfrac{f^2}{gH}}, \tag{3}$$

where $\beta = (f\alpha)/H$, f is the Coriolis parameter, g is the gravity, and $H = H_0 - (\alpha L)/2$ is the average depth of the slope stretch. For the one-dimensional topography [(1)], the boundary conditions restrict which wavenumbers are possible in the y direction (i.e., the eigenvalues). For the boundary conditions

$$\begin{aligned} v &= 0 \quad \text{at} \quad y = 0 \\ \frac{\partial v}{\partial y} &= 0 \quad \text{at} \quad y = L, \end{aligned} \tag{4}$$

the solution (2) is valid for

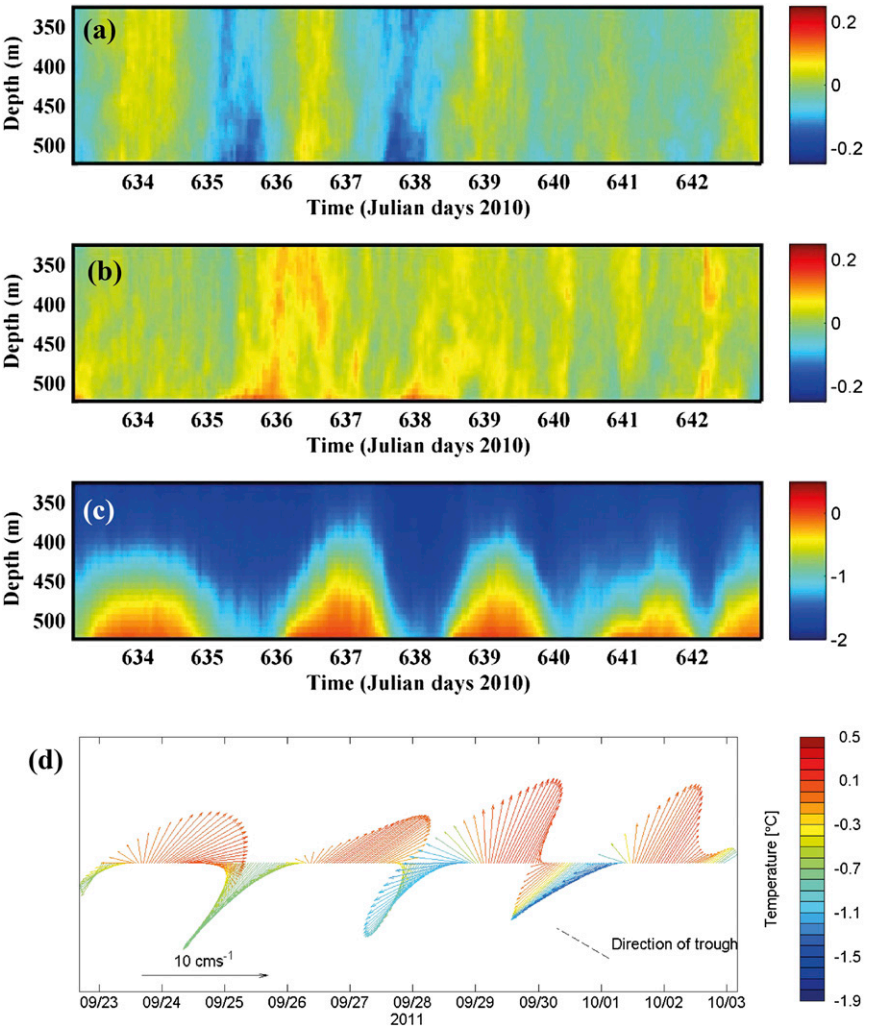

FIG. 5. Oscillations in velocity and temperature. (a) Detided across-trough velocity component. (b) Detided along-trough velocity component. (c) Temperature. (d) Quiver plot showing low-passed velocity anomalies from S2, 100 mab. The velocity scale is given in the lower-left corner and the color of the arrow indicates the temperature at 100 mab. The dashed, black line indicates the direction of the trough. Dates are given in the format month/day.

$$l_n = \left(n + \frac{1}{2}\right)\frac{\pi}{L}, \tag{5}$$

where n signifies the mode number starting at zero so that the first mode is given by $l_0 = 0.5(\pi/L)$ and the second is given by $l_1 = 1.5(\pi/L)$.

A code for determining the eigenfunctions and modal structures numerically for a real topography and stratification was presented in Brink (2006; see also http://www.whoi.edu/page.do?pid=23361), assuming an inviscid sea and a linear wave equation. Figure 7b shows the surface signature of the first and second modes for the Brink model, using the real topography in Fig. 7a and the measured stratification during a cruise to the region in 2010 (Ha et al. 2014) together with the analytical solution [(2)] using boundary conditions from (4).

The eigenfunction over the real topography (solid lines, Figs. 7a,b) has the surface signature of the wave concentrated to the steeper parts of the slope, while the simplified solution (dashed lines, Figs. 7a,b) has the wave spread evenly (sinusoidal) over the slope. Apart from this the surface signature is qualitatively similar for the two solutions. The introduction of stratification does not change the solution in any significant way, and the surface signature for the solution with stratification and without are indistinguishable. This is expected since the Burger number, that is, $\mathrm{Bu} = (N^2\alpha^2)/f^2$ (where N is the buoyancy frequency, α is the bottom slope, and

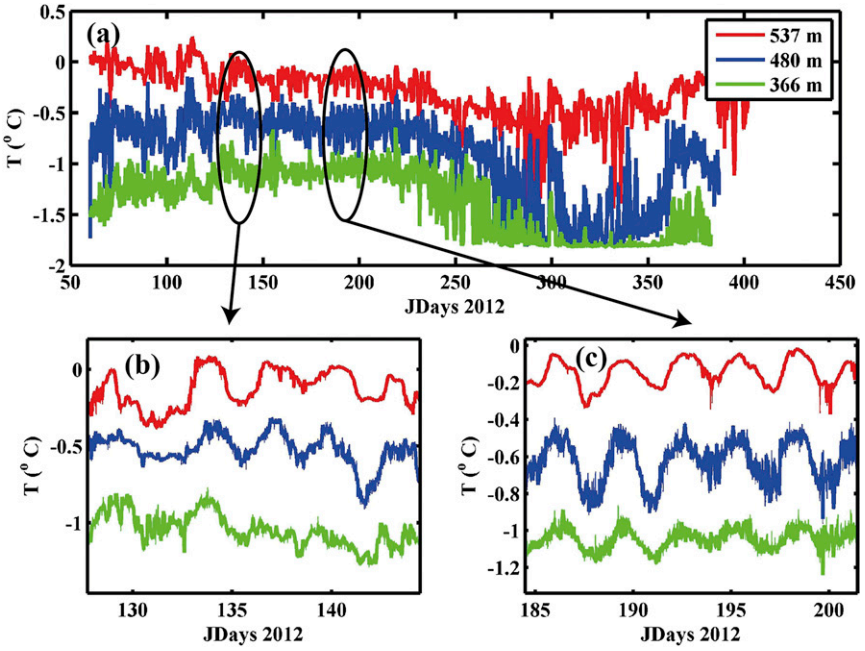

FIG. 6. Time series of temperature from the three MicroCATs at mooring S3. For location of the mooring see Fig. 1 and Table 1. (a) Complete record. (b) Example of oscillations occurring between days 128–145. (c) Example of oscillations occurring between days 185–202. Color indicates MicroCAT depth according to the legend in (a).

f is the Coriolis frequency) is less than 0.1. It was shown in Brink (2006) that for Bu < 1 the relative importance of stratification is small compared to the shelf geometry, and the solutions are similar to the barotropic solutions.

Equation (3) gives the dispersion relation for a free Rossby wave on a constant bottom slope. The corresponding relation can also be calculated numerically from the Brink (2006) model, using the boundary condition of (4). Figure 8 shows the numerical solution together with the result from (3) for the first two modes.

From the dispersion relation, the group velocity in the x direction c_X is given by

$$c_X = \frac{d\omega}{dk},$$

or [using (3)],

$$c_X = \frac{\beta\left(k^2 - l^2 - \dfrac{f^2}{gH}\right)}{\left(k^2 + l^2 + \dfrac{f^2}{gH}\right)^2}. \tag{6}$$

Since the topographic variations in the study region are $O(100)$ km or smaller, we have that $k^2 \gg f^2/(gH)$ and $l^2 \gg f^2/(gH)$ (using $k, l \geq 1/10^5$, $f \sim 1.4 \times 10^{-4}\,\mathrm{s}^{-1}$, and $H \sim 500$ m). Equations (3) and (6) can then be approximated by

$$\omega \simeq -\frac{\beta k}{k^2 + l^2}, \quad \text{and} \tag{7}$$

$$c_X \simeq \frac{\beta(k^2 - l^2)}{(k^2 + l^2)^2}. \tag{8}$$

Equation (8) tells us that for short waves, energy propagates with the coast on the right-hand side, that is, southeastward in the present topography (Fig. 1). The energy in long waves (i.e., small k) propagates with shallow water on the left. When the wavelength in the x direction is approximately equal to the wavelength in the y direction, we have that $k \approx l$ and $c_X \simeq 0$. Then the energy does not move away, and there will be resonance if waves are formed in, or transmitted into, the area. The approximate frequency ω_R of the resonant oscillations is given by [using (8) and (5)]

$$\omega_R \approx \frac{\beta}{2l_n}, \quad \text{or} \quad \omega_R \approx \frac{\beta L}{\pi(2n+1)}, \tag{9}$$

where $n = 0$ for the first mode and $n = 1$ for the second. Using $\beta = (f\alpha)/H$, the resonant frequency can hence be written

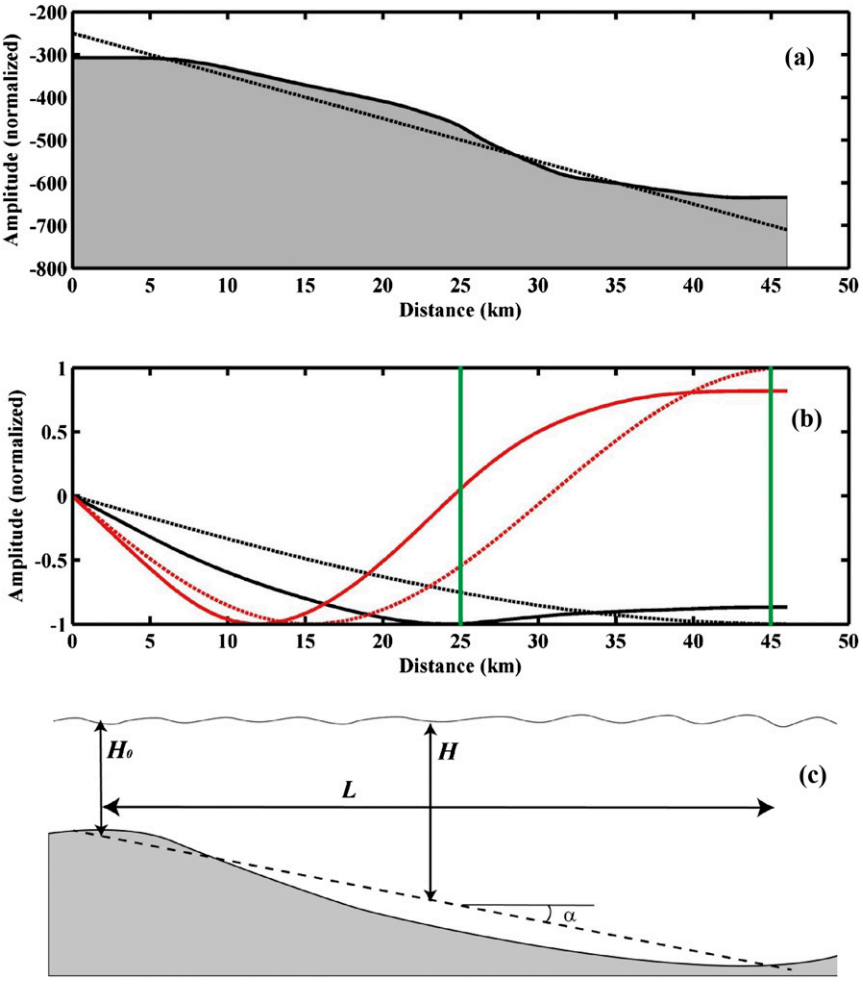

FIG. 7. (a) Real topography (shaded area) as measured by multibeam on the IB *Oden* during a cruise to the region in 2010, together with a straight dotted line representing the simplified topography used for analytical solutions. (b) The mode structures obtained from the analytical solution (dotted lines) and the numerical solution obtained using the real bathymetry and stratification (solid lines). The black lines show the first mode; the red lines show the second mode. (c) Sketch showing the topographic parameters in the analytical expressions and for the calculations of the resonant frequencies in Table 2.

$$\omega_R \approx \frac{f\alpha}{\pi}\frac{L}{H} \tag{10}$$

for the first mode, where f is the Coriolis parameter, α is the bottom slope, L is the length of the slope stretch, and H is the average depth. (Figure 7c shows a sketch of the topographic parameters. Note that H/L is in general not equal to α.)

The observed spectrum peak for the S2 mooring (Fig. 3) lies close to the frequency where topographic Rossby waves have zero group velocity (Fig. 8), suggesting that the observed oscillations might be resonant Rossby waves. These oscillations appear not to affect the average northwestward flow of water; the wavelet analysis (Fig. 4) shows that oscillations of the period around 64 h or shorter have strong variability but that peaks of energy around this frequency are not coinciding with peaks of energy in lower frequency.

Using the simplified expression [(9)] and topographic parameters (Fig. 7c) relevant for the three moorings (Table 2), it is seen that the fastest resonant oscillations are occurring at S2 and slower ones (period 83 h) are expected at S3. The observations show broad subinertial peaks centered on somewhat lower frequencies at S3 than S2, in qualitative agreement with the analytical expression (Fig. 3). For S1 the first-mode resonant period is 157 h (6.5 days), likely too slow to permit free waves to form. The wind forcing often changes

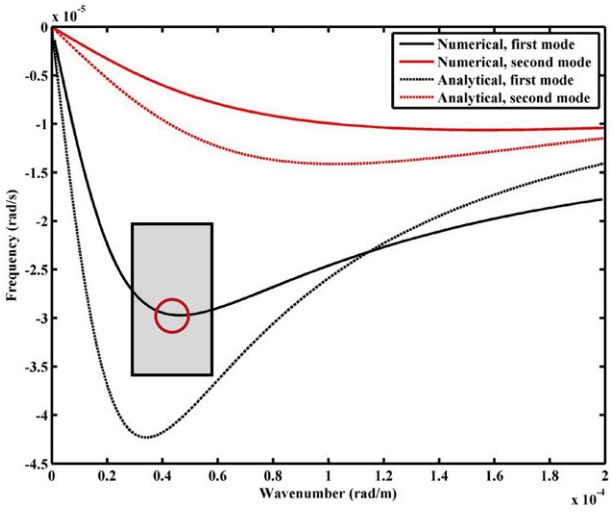

FIG. 8. Dispersion relation for the analytical solution (dotted lines) and the numerical solution based on real topography and stratification (solid lines). Black lines show first mode; red lines show second mode. The shaded square indicates the frequency boundaries of the observed spectrum peak (see Fig. 3) and the wavelength boundaries (green lines in Fig. 7). Red circle indicate the zero group velocity frequency–wavelength combination used.

sign during 157 h, and in addition the oscillations are slow enough for frictional damping to be effective (Brink 2006). Nonetheless, on occasions, a slow oscillation resembling the persistent ones at S2 and S3 can be seen also in S1.

5. Discussion

The high coherence (0.69) between wind and cross-shelf velocity for a 67-h period suggests that the observed oscillations are resonant topographic Rossby waves triggered by the wind. A similar resonant interaction has, for example, been observed on the Scottish continental shelf when storms created topographic Rossby waves along the slope (Gordon and Huthnance 1987) and on the southern slope of the Iceland–Faroe Ridge (Miller et al. 1996). The fact that they are so clearly observed in the present study is somewhat surprising, given that no previous reports of resonant topographic Rossby waves have been made from the Antarctic continental shelf. An explanation can be that the topography in this area is steep and shallow, such that the first-mode Rossby wave has a comparatively high resonant frequency. Semiregular oscillations with distinct subinertial periods have, however, been found, for example, in the Weddell Sea (Darelius et al. 2009; Jensen et al. 2013) and are not inconsistent with the theory of resonant topographic Rossby waves.

The measurements at S2 show (Fig. 2; see also Ha et al. 2014) that in addition to the resonant waves there is a more slowly varying current out from the shelf, transporting water and heat away from the continent (Ha et al. 2014). However, at any one time the velocity and temperature field is completely dominated by the Rossby waves oscillating on a 60–80-h time scale. The oscillations are comparable, or even larger, in magnitude to tides (Fig. 3). Single CTD and LADCP measurements are hence of limited value in this region. To get an estimate of quantities important for oceanic heat flux to glaciers, such as warm layer thickness, heat transport, or bottom temperature, it is imperative to measure during at least one Rossby cycle (i.e., about 80 h). This is particularly important when drawing conclusions of long-term trends based on sparse CTD measurements.

It is also important to distinguish these resonant Rossby waves from eddies. Both waves and eddies have oscillations in velocity and temperature–salinity, although eddies are less regular. However, eddies arise from an instability in the main flow and act to transport fluid parcels across gradients in depth, density, or velocity to ultimately stabilize the flow. For example, eddy-induced transport is a primary contributor to mass and property fluxes across the slope in the west Antarctic Peninsula (see, e.g., Thompson et al. 2014; Moffat et al. 2009; Martinson and McKee 2012). Single linear Rossby waves on the other hand are triggered by external events, for example wind bursts, and have no impact on the mean flow. Hence, although there is a clear correlation between velocity and temperature, the waves found in the present study do not induce any net oceanic heat flux toward or away from the coast. This is expected since waves per definition do not move any fluid and have closed streamlines. If

TABLE 2. Approximate topographic parameters for the three mooring sites based on bathymetric data from the International Bathymetric Chart of the Southern Ocean (IBCSO) database (Arndt et al. 2013). In the table, α denotes bottom slope, L denotes distance between the trough crest and the trough bottom, and H_0 is the depth at the trough crest (see sketch in Fig. 7c). Also shown are the calculated frequencies ω_R for the first two modes of resonant topographic Rossby waves [(10)] and the corresponding periods T_R.

Mooring	α	L (km)	H_0 (m)	H (m)	ω_R^1 (rad s^{-1})	ω_R^2 (rad s^{-1})	T_R^1 (h)	T_R^2 (h)
S1	0.001	100	350	400	1.1×10^{-5}	3.7×10^{-6}	157	470
S2	0.01	45	250	475	4.2×10^{-5}	1.4×10^{-5}	41	124
S3	0.005	45	370	480	2.1×10^{-5}	6.7×10^{-6}	83	250

the waves break, for example, when they encounter small-scale topography, or under wave–wave interaction, a net transport in the cross-shelf direction can be induced (e.g., St-Laurent et al. 2013). Such effects are, however, second order compared to the pronounced lifting/dropping of the thermocline that the oscillations themselves induce.

Acknowledgements. Logistic support for this work was provided by the Korea Polar Research Institute (KOPRI) and carried out on the Korean RVIB *Araon*. The authors are grateful for expert assistance from the captain and crew onboard *Araon*. The research was supported by the National Research Foundation of Korea (NRF) Grant 2015K2A3A1000201, the K-Polar Program (PP15020) of KOPRI, the STINT Korea–Sweden Research Cooperation (KO2014-5825), and the Swedish Research Council.

REFERENCES

Arndt, J. E., and Coauthors, 2013: The International Bathymetric Chart of the Southern Ocean (IBCSO) version 1.0—A new bathymetric compilation covering circum-Antarctic waters. *Geophys. Res. Lett.*, **40**, 3111–3117, doi:10.1002/grl.50413.

Arneborg, L., A. K. Wåhlin, G. Björk, B. Liljebladh, and A. H. Orsi, 2012: Persistent inflow of warm water onto the central Amundsen shelf. *Nat. Geosci.*, **5**, 876–880, doi:10.1038/ngeo1644.

Bracegirdle, T. J., and G. J. Marshall, 2012: The reliability of Antarctic tropospheric pressure and temperature in the latest global reanalyses. *J. Climate*, **25**, 7138–7146, doi:10.1175/JCLI-D-11-00685.1.

Brink, K., 2006: Coastal-trapped waves with finite bottom friction. *Dyn. Atmos. Oceans*, **41**, 172–190, doi:10.1016/j.dynatmoce.2006.05.001.

Darelius, E., L. Smedsrud, S. Österhus, A. Foldvik, and T. Gammelsröd, 2009: Structure and variability of the Filchner overflow plume. *Tellus*, **61A**, 446–464, doi:10.1111/j.1600-0870.2009.00391.x.

Dee, D. P., and Coauthors, 2011: The ERA-Interim reanalysis: Configuration and performance of the data assimilation system. *Quart. J. Roy. Meteor. Soc.*, **137**, 553–597, doi:10.1002/qj.828.

Gill, A. E., 1982: *Atmosphere–Ocean Dynamics.* Academic Press, 662 pp.

Gordon, R. L., and J. M. Huthnance, 1987: Storm-driven continental shelf waves over the Scottish continental shelf. *Cont. Shelf Res.*, **7**, 1015–1048, doi:10.1016/0278-4343(87)90097-5.

Ha, H. K., and Coauthors, 2014: Circulation and modification of warm deep water on the central Amundsen Shelf. *J. Phys. Oceanogr.*, **44**, 1493–1501, doi:10.1175/JPO-D-13-0240.1.

Jacobs, S., A. Jenkins, C. Giulivi, and P. Dutrieux, 2011: Stronger ocean circulation and increased melting under Pine Island Glacier ice shelf. *Nat. Geosci.*, **4**, 519–523, doi:10.1038/ngeo1188.

Jenkins, A., P. Dutrieux, S. Jacobs, S. McPhail, J. Perrett, A. Webb, and D. White, 2010: Observations beneath Pine Island Glacier in West Antarctica and implications for its retreat. *Nat. Geosci.*, **3**, 468–472, doi:10.1038/ngeo890.

Jensen, M. F., I. Fer, and E. Darelius, 2013: Low frequency variability on the continental slope of the southern Weddell Sea. *J. Geophys. Res. Oceans*, **118**, 4256–4272, doi:10.1002/jgrc.20309.

Martinson, D. G., and D. C. McKee, 2012: Transport of warm Upper Circumpolar Deep Water onto the western Antarctic Peninsula continental shelf. *Ocean Sci.*, **8**, 433–442, doi:10.5194/os-8-433-2012.

Miller, A. J., P. F. J. Lermusiaux, and P.-M. Poulain, 1996: A topographic Rossby-mode resonance over the Iceland–Faeroe Ridge. *J. Phys. Oceanogr.*, **26**, 2735–2747, doi:10.1175/1520-0485(1996)026<2735:ATMROT>2.0.CO;2.

Moffat, C., B. Owens, and R. C. Beardsley, 2009: On the characteristics of Circumpolar Deep Water intrusions on the west Antarctic Peninsula continental shelf. *J. Geophys. Res.*, **114**, C05017, doi:10.1029/2008JC004955.

Padman, L., A. J. Plueddemann, R. D. Muench, and R. Pinkel, 1992: Diurnal tides near the Yermak Plateau. *J. Geophys. Res.*, **97**, 12 639–12 652, doi:10.1029/92JC01097.

St-Laurent, P., J. Klinck, and M. Dinniman, 2013: On the role of coastal troughs in the circulation of warm Circumpolar Deep Water on Antarctic shelves. *J. Phys. Oceanogr.*, **43**, 51–64, doi:10.1175/JPO-D-11-0237.1.

Thompson, A., 2008: The atmospheric ocean: Eddies and jets in the Antarctic Circumpolar Current. *Philos. Trans. Roy. Soc.*, **A366**, 4529–4541, doi:10.1098/rsta.2008.0196.

——, K. J. Heywood, S. Schmidtko, and A. L. Stewart, 2014: Eddy transport as a key component of the Antarctic overturning circulation. *Nat. Geosci.*, **7**, 879–884, doi:10.1038/ngeo2289.

Thomson, D. J., 1982: Spectrum estimation and harmonic analysis. *Proc. IEEE*, **70**, 1055–1096, doi:10.1109/PROC.1982.12433.

Torrence, C., and G. Compo, 1998: A practical guide to wavelet analysis. *Bull. Amer. Meteor. Soc.*, **79**, 61–78, doi:10.1175/1520-0477(1998)079<0061:APGTWA>2.0.CO;2.

Wåhlin, A. K., X. Yuan, G. Björk, and C. Nohr, 2010: Inflow of warm Circumpolar Deep Water in the central Amundsen shelf. *J. Phys. Oceanogr.*, **40**, 1427–1434, doi:10.1175/2010JPO4431.1.

——, and Coauthors, 2013: Variability of warm deep water inflow in a submarine trough on the Amundsen Sea shelf. *J. Phys. Oceanogr.*, **43**, 2054–2010, doi:10.1175/JPO-D-12-0157.1.

Walker, D. P., M. A. Brandon, A. Jenkins, J. T. Allen, J. A. Dowdeswell, and J. Evans, 2007: Oceanic heat transport onto the Amundsen Sea shelf through a submarine glacial trough. *Geophys. Res. Lett.*, **34**, L02602, doi:10.1029/2006GL028154.